Materials Transactions, Vol. 52, No. 4 (2011) pp. 586 to 590
Special Issue on Advanced Materials for Hydrogen Energy Applications

Phase Transformation and Lattice-Strain Formation in $Ti_{1.0}V_{1.1}Mn_{0.9}$ during First Absorption and Desorption

Saishun Yamazaki, Jin Nakamura*[1], Kouji Sakaki, Yumiko Nakamura*[2] and Etsuo Akiba

National Institute of Advanced Industrial Science and Technology (AIST), Tsukuba 305-8565, Japan

We used powder X-ray diffraction (XRD) and Rietveld refinement to study phase transformation and the lattice strain introduced into each hydride phase of $Ti_{1.0}V_{1.1}Mn_{0.9}$ during first absorption and desorption. Hydrogenation proceeded from a solid-solution phase to a dihydride phase via a monohydride phase. Each single-phase region was observed beside two clear plateau regions on the pressure–composition (*P–C*) isotherm. In contrast, the desorption *P–C* isotherm showed only one clear plateau, corresponding to a two-phase region of the dihydride and the monohydride. The plateau was connected to a two-phase region of the monohydride and a solid-solution phase, and to another region of solid-solution phases. The monohydride single-phase region was not clearly observed during desorption. Isotropic lattice strain was introduced, and increased with phase transformation during the first absorption. The strain increased further in the subsequent phase transformation during desorption, particularly upon formation of a solid-solution phase. [doi:10.2320/matertrans.MA201004]

(Received October 4, 2010; Accepted December 16, 2010; Published April 1, 2011)

Keywords: *hydrogen storage, BCC solid-solution alloy, phase transformation, lattice strain, X-ray diffraction*

1. Introduction

Ti- or V-based solid-solution alloys with a BCC structure have been studied as promising hydrogen-storage materials since the hydrogenation properties of Ti–V–Mn and Ti–V–Cr alloys were reported.[1–3] BCC solid-solution alloys with a composition close to $Ti_{1.0}V_{1.1}Mn_{0.9}$ form three hydrogenated phases between 0.001 and 5.0 MPa of H_2 at moderate temperatures.[4,5] The crystal structure changes from BCC to pseudo-cubic FCC, one axis of which is shorter than the others by a few percent, and then to FCC, with increasing hydrogen content, along the absorption pressure–composition (*P–C*) isotherm; the isotherm has two clear plateaus. The shape of the desorption *P–C* isotherm is different from that of the absorption isotherm. Detailed structural changes along the desorption isotherm have not been investigated.

The peaks in the X-ray diffraction (XRD) patterns for Ti–V–Mn hydride phases broadened during hydrogenation.[4] This broadening was supposed to be due to lattice strain. Lattice strain accompanied by hydrogenation has been studied for $LaNi_5$-based compounds by X-ray and neutron diffraction,[6–9] positron annihilation,[10,11] and transmission electron microscopy (TEM).[12,13] *In-situ* X-ray and neutron diffraction measured along the *P–C* isotherm showed that lattice strain is introduced upon phase transformation, i.e., transition from the solid-solution phase to the hydride phase.[6,8] The anisotropic strain in the diffraction peaks[6–9] has the same orientation as the Burgers dislocation vectors observed by TEM,[12,13] indicating that in this case the strain is accompanied by dislocations. Strain formation, which is closely related to defect formation, is worth noting because it is related to hydrogenation properties, e.g., hysteresis in the *P–C* isotherm, cyclic stability.[12] By analogy with $LaNi_5$-based compounds, phase transformation in BCC solid-solution alloys is also expected to cause strain formation, which affects hydrogenation properties. The way in which lattice strain is introduced in each phase transformation during both absorption and desorption is of interest.

In this study, we investigated the hydride phases of $Ti_{1.0}V_{1.1}Mn_{0.9}$ formed during the first absorption and desorption along the *P–C* isotherm, using XRD to clarify phase transformations and lattice-strain formation. We focused on the first absorption and desorption because lattice defects are introduced in particular in the initial hydrogenation process. Rietveld refinement including profile analysis provided the structure of the metal sub-lattice and the lattice strain for each hydride phase.

2. Experimental Details

2.1 Alloys preparation

Alloy ingots were prepared by arc-melting. The morphologies and chemical compositions were examined using scanning electron microscopy (SEM) and energy dispersive X-ray spectroscopy (EDX). The SEM images were homogeneous and the average composition was $Ti_{1.0}V_{1.1}Mn_{0.9}$ for all the ingots. The as-cast ingots were roughly crushed into powders of particle size $\sim$100 μm.

2.2 *P–C* isotherm measurements and preparation of hydride samples

Powder samples were sealed in a stainless-steel container and evacuated at 723 K for 4 h. The *P–C* isotherms were measured by the Sieverts method at 353 K. Hydride samples were prepared by first hydrogen absorption and desorption along the *P–C* isotherms. The measurements were stopped at selected hydrogen contents and then the samples were deactivated with acetone.

2.3 XRD measurements

XRD was performed using a diffractometer (Rigaku, RINT-2500V) with Cu Kα radiation. The voltage and current used for the measurements were 50 kV and 200 mA.

*[1]Present address: Japan Metals & Chemicals Co., Ltd., Nishiokitama-gun, Yamagata 999-1351, Japan
*[2]Corresponding author, E-mail: yumiko.nakamura@aist.go.jp

2.4 Peak profile analysis

The diffraction profiles were analyzed using a Rietveld refinement program RIETAN-2000.[14] A pseudo-Voigt function[15] is used for expressing peak profiles, and the FWHM (full-widths at half-maximum) of the Gaussian and Lorentzian parts, H_{KG} and H_{KL}, are expressed as follows:[16]

$$H_{KG} = [8 \ln 2(U \tan^2 \theta_K + V \tan \theta_K + W)]^{1/2}:$$
Gaussian part

$$H_{KL} = (X + X_e \cos \phi_K) \sec \theta_K + (Y + Y_e \cos \phi_K) \tan \theta_K:$$
Lorentzian part

where θ_K is the Bragg angle; V and W in the Gaussian part are instrument-dependent parameters; X and X_e in the Lorentzian part are crystallite-size-effect parameters; U, Y, and Y_e are parameters expressing peak broadening caused by crystal lattice strain, which corresponds to local variations in lattice spacing; U and Y are isotropic strain parameters; Y_e is an anisotropic strain parameter; and ϕ_K is the angle between the scattering vector and an anisotropic peak-broadening axis. The axis is represented by a vector of the simplest component. In this analysis, V and W were fixed at the parameters for Si as a standard sample for analyzing instrument effects. X_e and Y_e were fixed at zero because anisotropic peak broadening related to these parameters was not observed. The crystallite size and lattice strain were evaluated by the following equations:[16]

$180K\lambda/\pi X$: crystallite size

$(\pi/180)[8 \ln 2(U - U_i)]1/2 \times 100(\%)$:
lattice strain from the Gaussian part

$(\pi/180)(Y - Y_i) \times 100(\%)$:
lattice strain from the Lorentzian part

where K is the Scherrer constant ($K = 0.9$); λ is the X-ray wavelength; and U_i and Y_i are instrumental contributions, which were obtained from analysis of Si data. The lattice-strain values mentioned below are sums of the values obtained from the Gaussian part and the Lorentzian part. The values correspond to the distribution width in the lattice spacing divided by the average spacing.

The degree of refinement is judged by the goodness of fit, s:

$$s = R_{wp}/R_e$$

where R_{wp} is the weighted sum of the residuals of the least-squares fit and R_e is the statistically expected value.

3. Results and Discussion

Figure 1 shows the first absorption and desorption P–C isotherms for $Ti_{1.0}V_{1.1}Mn_{0.9}$. The absorption isotherm clearly showed two plateau regions, one from 0.5 to 0.8 H/M and the other from 1.0 to 1.6 H/M. In contrast, the desorption isotherm showed only one clear plateau, between 1.0 and 1.6 H/M, and an unclear sloping curve from 1.0 H/M to 0.5 H/M directly connected to the plateau.

A solid-solution phase (A1: $Ti_{1.0}V_{1.1}Mn_{0.9}H_{1.2}$), a monohydride phase (A2: $Ti_{1.0}V_{1.1}Mn_{0.9}H_{2.8}$), and a dihydride phase (A3: $Ti_{1.0}V_{1.1}Mn_{0.9}H_{5.4}$) were obtained during the first absorption under the conditions indicated in Fig. 1. These phases had a BCC structure, a pseudo-cubic FCC structure, and an FCC structure, respectively. These results agree with our previous report.[4] The results of Rietveld refinement are shown in Fig. 2 and Table 1. Note that the monohydride, which was shown to have a pseudo-cubic FCC structure, has the same symmetry as a BCT structure (space group: I4/mmm), but the c/a ratio, around 1.3, is closer to $\sqrt{2}$ for an FCC structure than the value of ~1.1 reported for the BCT structure of monohydrides of V metals/alloys (e.g., β-$VH_{0.5}$). This is why the monohydride structure is called pseudo-cubic FCC. The previous report showed that the ratio for this monohydride ranged from 1.29 to $\sqrt{2}$, depending on the alloy composition. The C14 Laves phase observed in the XRD patterns was taken into the refinement model to obtain a better fit. The fraction of the C14 Laves phase was several percent or less. The fluctuations of the fraction among the samples are within the refinement error.

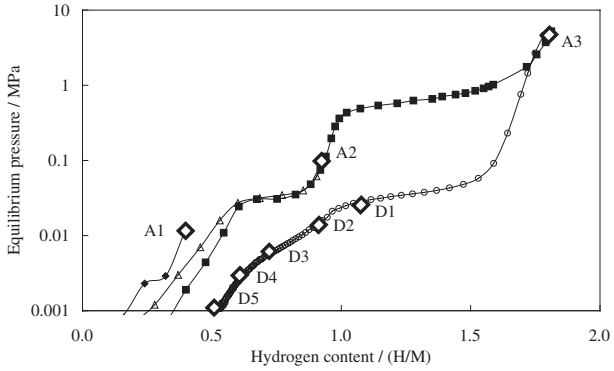

Fig. 1 P–C isotherms of $Ti_{1.0}V_{1.1}Mn_{0.9}$, measured at 353 K, for preparing hydride samples.

Five samples, D1–D5 in Fig. 1, were prepared during the first desorption. The XRD data obtained for D2–D5 are shown in Fig. 3. The hydride samples D1 ($Ti_{1.0}V_{1.1}Mn_{0.9}H_{3.3}$) and D2 ($Ti_{1.0}V_{1.1}Mn_{0.9}H_{2.8}$) contained both monohydride and dihydride phases; a difference was found only in the phase fraction.

Sample D3 ($Ti_{1.0}V_{1.1}Mn_{0.9}H_{2.2}$) showed heavily broadened peaks. The monohydride phase remained, but the peak positions of the pseudo-cubic FCC structure shifted to a higher 2θ. In particular, the 111 and 200 peaks in the bottom part were too broad to fit the model of a single monohydride phase. The Rietveld analysis was therefore carried out with a two-phase model containing the monohydride phase and another phase with a BCT structure. Sample D4 ($Ti_{1.0}V_{1.1}Mn_{0.9}H_{1.9}$) also showed a broad and asymmetric peak profile. Fitting of the pattern needed a model containing two BCT phases. The subsequent desorption led to the hydride D5 ($Ti_{1.0}V_{1.1}Mn_{0.9}H_{1.6}$), which had a BCT structure and sharper peaks than those of D4. The cell volume was calculated for all the samples, as shown in Table 1 and Fig. 4. The BCT phases observed in samples D3–D5 had cell volumes ($30–31 \times 10^{-3}$ nm^3) which were smaller than those of the monohydrides ($\sim 32 \times 10^{-3}$ nm^3) and closer to that of the solid-solution phase obtained in absorption (30×10^{-3} nm^3 for A1). The BCT phases observed in samples D3–D5 were therefore assumed to be solid-solution phases. The

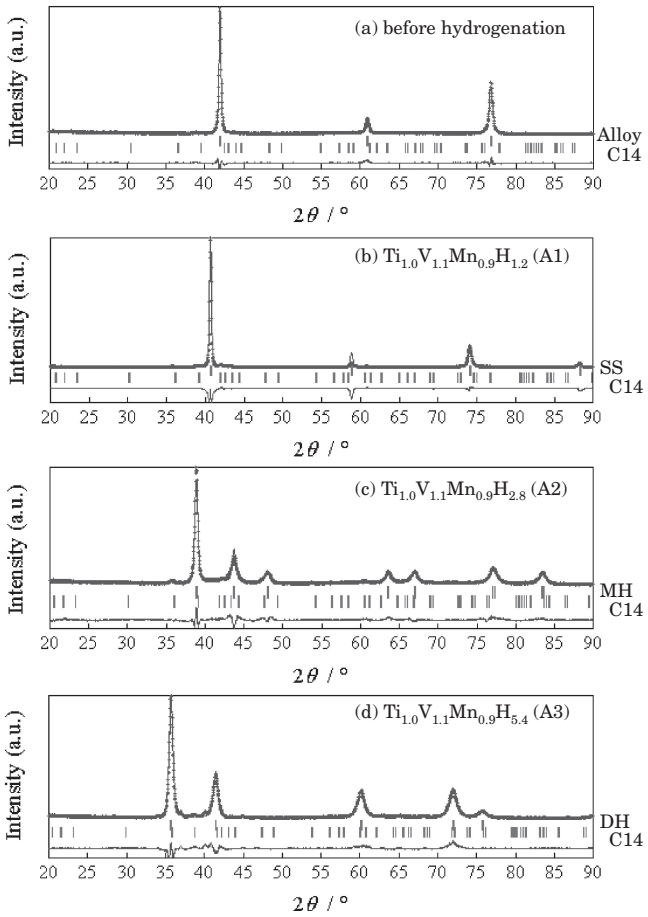

Fig. 2 XRD profiles for $Ti_{1.0}V_{1.1}Mn_{0.9}$ alloy and hydride samples obtained during the first absorption. (a) before hydrogenation, (b) $Ti_{1.0}V_{1.1}Mn_{0.9}H_{1.2}$ (A1, 0.39 H/M), (c) $Ti_{1.0}V_{1.1}Mn_{0.9}H_{2.8}$ (A2, 0.92 H/M), and (d) $Ti_{1.0}V_{1.1}Mn_{0.9}H_{5.4}$ (A3, 1.81 H/M). SS: solid-solution phase, MH: monohydride phase, DH: dihydride phase, C14: C14 Laves phase.

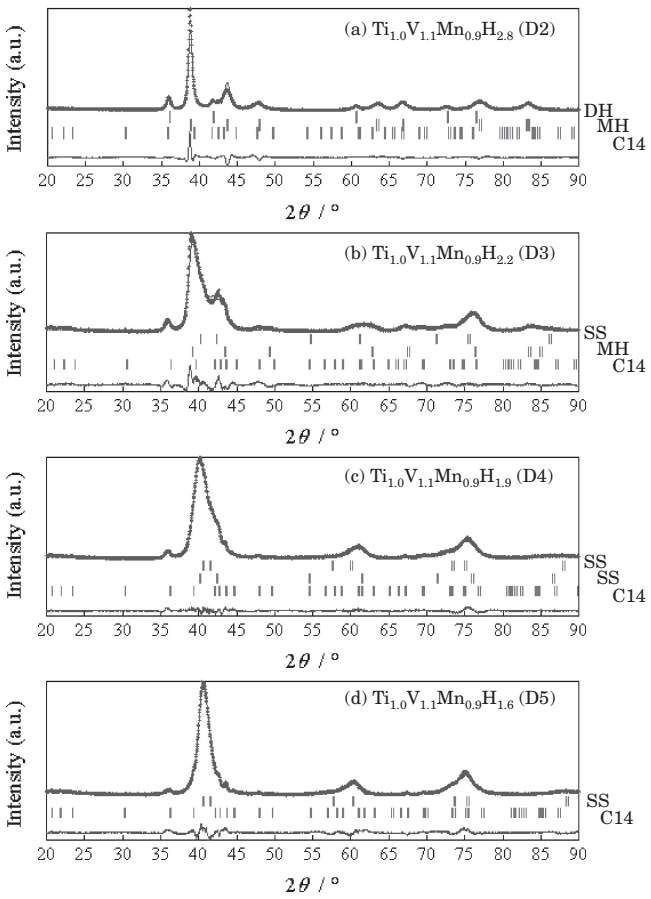

Fig. 3 XRD profiles for $Ti_{1.0}V_{1.1}Mn_{0.9}$ hydride samples during the first desorption. (a) $Ti_{1.0}V_{1.1}Mn_{0.9}H_{2.8}$ (D2, 0.95 H/M), (b) $Ti_{1.0}V_{1.1}Mn_{0.9}H_{2.2}$ (D3, 0.74 H/M), (c) $Ti_{1.0}V_{1.1}Mn_{0.9}H_{1.9}$ (D4, 0.63 H/M), and (d) $Ti_{1.0}V_{1.1}Mn_{0.9}H_{1.6}$ (D5, 0.52 H/M). SS: solid-solution phase, MH: monohydride phase, DH: dihydride phase, C14: C14 Laves phase.

c/a ratios of the BCT phases were about 1.1 (in samples D3 and D4) and 1.04 (in samples D4 and D5); this supports the assignment of BCT phases to the solid-solution phases. The obtained cell volumes and c/a ratios suggest that there are two solid-solution phases with different hydrogen contents, and that they coexist in sample D4. The c/a ratios of the monohydride phases were around 1.3 for samples A2, D1, and D2, where the monohydride coexists with the dihydride, but the ratio decreased to 1.25 for D3, where the monohydride coexists with a solid-solution phase.

The desorption *P–C* isotherm showed one clear plateau between 1.0 and 1.6 H/M and an unclear sloping curve from 1.0 H/M to 0.5 H/M, where the hydrogen content slowly decreased with decreasing hydrogen pressure. In the latter part, no clear single-phase region was observed, although a monohydride single-phase region appeared between the two plateaus in absorption. Structural analysis indicated that in this region the phase transforms from coexistence of the dihydride phase and monohydride phase (~0.9–1.6 H/M), via coexistence of the monohydride phase and a solid-solution phase (~0.65–0.8 H/M), to two solid-solution phases (~0.55–0.65 H/M), and finally changes to a single solid-solution phase (Fig. 5). The phase-relation results suggested that a single monohydride phase may exist in a very narrow region between samples D2 and D3 (~0.8–

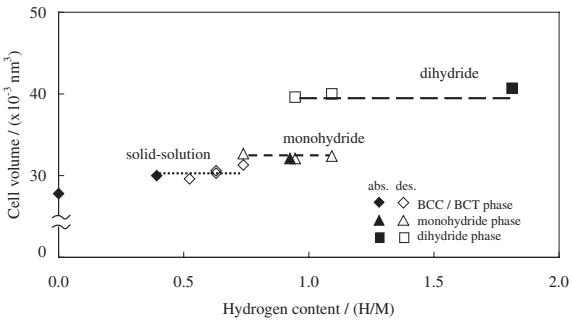

Fig. 4 Cell volumes for $Ti_{1.0}V_{1.1}Mn_{0.9}$ hydride samples. The cell volumes were calculated for BCT cells for all samples.

0.9 H/M). Assuming that sample D4 contains two solid-solution phases, the region where D4 is located should be a plateau region. However, the curve of the corresponding region is not as flat as that normally observed for a plateau. This is probably because the region is very narrow and the curve has a slope, reflecting the fact that hydrogen in the two solid-solution phases has a large stability distribution, as suggested by the large lattice strain mentioned below.

Figure 6 shows the isotropic lattice strain, evaluated by Rietveld analysis, plotted as a function of hydrogen content.

Table 1 Refined structural parameters for $Ti_{1.0}V_{1.1}Mn_{0.9}$ alloy and hydride samples. The sample numbers, A1–A3 and D1–D5, correspond to those indicated in Fig. 1.

Sample/phase	Space group	a (nm)	c (nm)	c/a	Fraction (%)	Cell volume ($\times 10^{-3}$ nm^3)*
absorption						
Before hydrogenation	*Im-3m*	0.3030(2)			98.4	27.8
C14 Laves phase	*P6$_3$/mmc*	0.489(1)	0.807(1)		1.6	
A1: $Ti_{1.0}V_{1.1}Mn_{0.9}H_{1.2}$						
solid-solution	*Im-3m*	0.31075(9)			94.5	30.0
C14 Laves phase	*P6$_3$/mmc*	0.4926(3)	0.809(1)		5.5	
A2: $Ti_{1.0}V_{1.1}Mn_{0.9}H_{2.8}$						
monohydride	*I4/mmm*	0.2917(2)	0.3776(2)	1.294	95.7	32.1
C14 Laves phase	*P6$_3$/mmc*	0.4974(5)	0.814(2)		4.3	
A3: $Ti_{1.0}V_{1.1}Mn_{0.9}H_{5.4}$						
dihydride	*Fm-3m*	0.4335(9)			99.7	40.7
C14 Laves phase	*P6$_3$/mmc*	0.4991(2)	0.821(3)		0.3	
desorption						
D1: $Ti_{1.0}V_{1.1}Mn_{0.9}H_{3.3}$						
dihydride	*Fm-3m*	0.43103(9)			34.0	40.0
monohydride	*I4/mmm*	0.29198(3)	0.37957(7)	1.299	63.8	32.4
C14 Laves phase	*P6$_3$/mmc*	0.4983(2)	0.812(3)		2.2	
D2: $Ti_{1.0}V_{1.1}Mn_{0.9}H_{2.8}$						
dihydride	*Fm-3m*	0.42931(7)			9.7	39.6
monohydride	*I4/mmm*	0.29152(5)	0.37799(8)	1.296	81.6	32.1
C14 Laves phase	*P6$_3$/mmc*	0.4983(2)	0.8045(9)		8.6	
D3: $Ti_{1.0}V_{1.1}Mn_{0.9}H_{2.2}$						
monohydride	*I4/mmm*	0.2971(9)	0.371(1)	1.249	33.4	32.7
solid-solution	*I4/mmm*	0.3046(9)	0.337(1)	1.106	64.1	31.3
C14 Laves phase	*P6$_3$/mmc*	0.4996(3)	0.81(1)		2.5	
D4: $Ti_{1.0}V_{1.1}Mn_{0.9}H_{1.9}$						
solid-solution	*I4/mmm*	0.3017(1)	0.3365(2)	1.115	40.5	30.6
solid-solution	*I4/mmm*	0.3080(1)	0.3200(3)	1.038	53.7	30.3
C14 Laves phase	*P6$_3$/mmc*	0.49532(7)	0.8135(6)		5.8	
D5: $Ti_{1.0}V_{1.1}Mn_{0.9}H_{1.6}$						
solid-solution	*I4/mmm*	0.3053(6)	0.3175(6)	1.039	92.9	29.6
C14 Laves phase	*P6$_3$/mmc*	0.490(1)	0.806(1)		7.1	

*The cell volume was calculated for the BCT cell for all the samples.

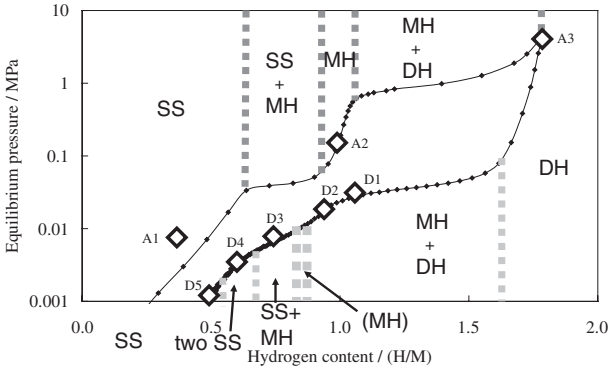

Fig. 5 Phase transformation for $Ti_{1.0}V_{1.1}Mn_{0.9}$ along the *P–C* isotherm for the first absorption and desorption at 353 K. SS: solid-solution phase, MH: monohydride phase, DH: dihydride phase.

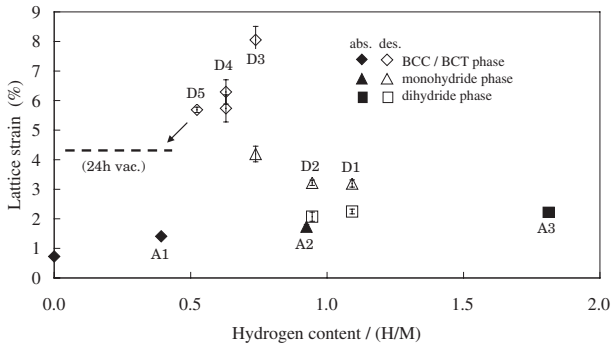

Fig. 6 Lattice strains for $Ti_{1.0}V_{1.1}Mn_{0.9}$ alloy and hydride samples obtained during the first absorption and desorption.

The lattice strain observed before hydrogenation was ~0.7%. This strain was originally introduced during sample preparation, particularly in crushing of the sample. The isotropic lattice strains of the solid-solution phase, the monohydride phase, and the dihydride phase during the first absorption were ~1.4%, ~1.7%, and ~2.2%, respectively, indicating that the lattice strain increased in proportion to the hydrogen content. Anisotropic strain was not observed.

During the first desorption, the lattice strains in sample D2 were ~3.2% for the monohydride phase and ~2.1% for the dihydride phase, respectively. The lattice strain of the solid-solution phase was ~8.1% in sample D3, but decreased to ~5.7% during desorption to sample D5. Another sample, which was evacuated for 24 h starting from the same conditions as those for D5, showed a strain of about 4.3%, as indicated in Fig. 6. During desorption, the lattice strain increased slightly on monohydride formation, and then increased significantly on formation of a solid-solution phase. The strain in the solid-solution phase gradually decreased with decreasing hydrogen content.

Some authors have reported that lattice defects were observed by TEM in a $Ti_{1.0}V_{1.1}Mn_{0.9}$ sample after hydrogenation.[17] This suggests that strain formation during absorption is probably due to the introduction of lattice defects. The strain introduced in the monohydride during desorption may also be due to lattice defects. In contrast, the strains observed in the solid-solution phases during desorption are caused not only by defect formation but also by another factor; the strain decreased with decreasing hydrogen content, although lattice defects generally do not migrate at 353 K. This strain can therefore be attributed to solved hydrogen in the solid-solution phases, e.g., inhomogeneous hydrogen distribution. The crystallite sizes evaluated from the parameter X were between ~30 nm and ~100 nm; the sizes tended to decrease with increasing hydrogen content during absorption. No clear tendency was observed in the values for desorption. The size effects on increasing the XRD peak widths were much smaller than the strain effects described above.

4. Conclusions

We investigated phase transformation and lattice-strain formation in $Ti_{1.0}V_{1.1}Mn_{0.9}$ along the first absorption and desorption P–C isotherm using Rietveld refinement of the XRD data, including profile analysis. Three hydrogenated phases, namely solid-solution, monohydride, and dihydride phases, were observed during both absorption and desorption. The phase transformation during desorption was unclear compared with the transformation observed during absorption. Desorption proceeded as follows: dihydride phase → dihydride and monohydride phases (→ monohydride phase) → monohydride phase and one solid-solution phase → two solid-solution phases → one solid-solution phase. A single monohydride phase for desorption may exist in the very narrow region between 0.8 and 0.9 H/M. The structure of the solid-solution phase changed with decreasing c/a ratio of the BCT cell. The isotropic lattice strain increased with phase transformation during absorption in proportion to the hydrogen content. This strain is probably a result of the introduction of lattice defects. The strain increased further in the subsequent phase transformation during desorption, reached a maximum in the solid-solution phase coexisting with the monohydride phase, and then decreased. The increase in lattice strain observed for the solid-solution phases can be attributed to inhomogeneous distribution of solved hydrogen.

Acknowledgments

This work was supported by the New Energy and Industrial Technology Development Organization (NEDO) under "Advanced Fundamental Research on Hydrogen Storage Materials (HYDRO-STAR)".

REFERENCES

1) J. Huot, E. Akiba and H. Iba: J. Alloy. Compd. **231** (1995) 181–187.
2) H. Iba and E. Akiba: J. Alloy. Compd. **231** (1995) 508–512.
3) E. Akiba and H. Iba: Intermetallics **6** (1998) 461–470.
4) Y. Nakamura and E. Akiba: J. Alloy. Compd. **311** (2000) 317–321.
5) Y. Nakamura and E. Akiba: J. Alloy. Compd. **345** (2002) 175–182.
6) Y. Nakamura and E. Akiba: J. Alloy. Compd. **308** (2000) 309–318.
7) Y. Nakamura, K. Oguro, I. Uehara and E. Akiba: J. Alloy. Compd. **298** (2000) 138–145.
8) M. P. Pitt, E. MacA. Gray, E. H. Kisi and B. A. Hunter: J. Alloy. Compd. **293–295** (1999) 118–123.
9) R. Černý, J.-M. Joubert, M. Latroche, A. Percheron-Guégan and K. Yvon: J. Appl. Crystallogr. **33** (2000) 997–1005.
10) K. Sakaki, H. Araki and Y. Shirai: Mater. Trans. **43** (2002) 1494–1497.
11) Y. Shirai, H. Araki, T. Mori, W. Nakamura and K. Sakaki: J. Alloy. Compd. **330–332** (2002) 125–131.
12) H. Inui, T. Yamamoto, M. Hirota and M. Yamaguchi: J. Alloy. Compd. **330–332** (2002) 117–124.
13) B. Décamps, J.-M. Joubert, R. Cerny and A. Percheron-Guégan: J. Alloy. Compd. **404–406** (2005) 570–575.
14) F. Izumi and T. Ikeda: Mater. Sci. Forum **321–324** (2000) 198–203.
15) P. Thompson, D. E. Cox and J. B. Hastings: J. Appl. Crystallogr. **20** (1987) 79–83.
16) A. C. Larson and R. B. Von Dreele: *GSAS–General Structure Analysis System*, Report No. LAUR 86-748, (Los Alamos National Laboratory, Los Alamos, 1994) pp. 127–138.
17) J. Matsuda, K. Asano, Y. Nakamura and E. Akiba: Abstracts of the Spring Meeting of the Japan Institute of Metals, (2010) p. 231 (in Japanese).